Supplementary Material

Comparison of Force Fields for the Prediction of Thermophysical Properties of Long Linear and Branched Alkanes

Sebastian Schmitt, Florian Fleckenstein, Hans Hasse,
and Simon Stephan

Laboratory of Engineering Thermodynamics (LTD),
RPTU Kaiserslautern, Kaiserslautern, Germany

simon.stephan@rptu.de

CONTENTS

S1. FINITE SIZE ANALYSIS

The finite size dependency of the results was analysed by conducting simulations of n-decane with the Potoff force field at T = 373.15 K and ρ = 0.66836 g/ml with six different box sizes that contained 200, 400 (used in this work for n-decane simulations), 1000, 2000, 5000, and 10000 molecules, respectively. For every box size, 20 replica simulations have been conducted and the procedure described in the main part of this work was applied to calculate the viscosity and the self-diffusion coefficient. The results of these simulations are given in Fig. S1 as function of the inverse box length $1/L$. For the viscosity, all results

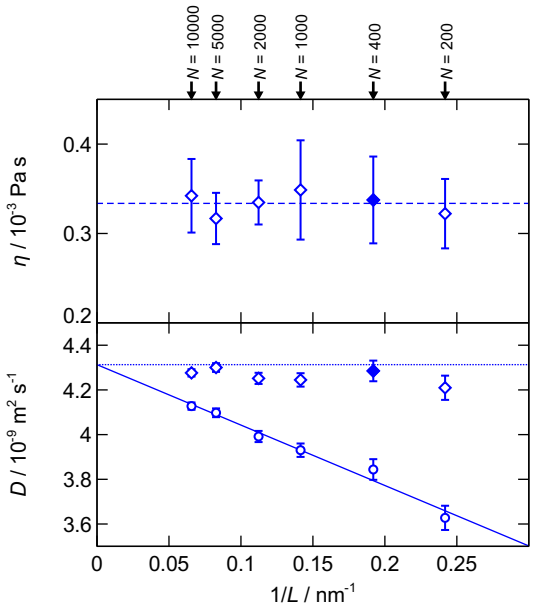

Figure S1. Viscosity η (top) and self-diffusion coefficient D (bottom) as function of the inverse box length $1/L$ of n-Decane at T = 373.15 K and ρ = 0.66836 g/ml calculated using the Potoff force field. Top: The dashed line represents the mean viscosity values as calculated from all box lengths. Bottom: The solid line represents a linear fit on the self-diffusion values and the dotted line the thermodynamic limit ($1/L$ = 0) as obtained from the linear fit. Filled symbols represent the values used in this work.

are within their error bars. Thus, there is no size dependency of the viscosity results. For the self-diffusion coefficient, it is known that there is a box size dependency when using the Einstein relation and a correction term was proposed[1]. In Fig. S1, the raw results without correction (circles) as well as the final values as used in this work (diamonds) are

shown. The thermodynamic limit ($L \to \infty$) can be calculated by extrapolating a linear fit on the uncorrected values to $1/L = 0$. The results in Fig. S1 show that the correction term produces good results in accordance with the result calculated from extrapolating to the thermondymic limit.

S2. CHOICE OF INTEGRATOR FOR ALL-ATOM SIMULATIONS

The all-atom force fields (excluding the reactive force fields) have been used with the RESPA multiple timestep integrator to reduce the computational costs of these simulations. The computational costs of all-atom force fields is in particular high as they usually use 3-4 times more interaction sites compared to united-atom force fields by nature. Additionally, they need a smaller time step as they include C-H bonds that obey high frequencies. To still conserve the total energy of the system, the time step has to be very small. This can be fixed by a multiple time step integrator like RESPA. Therefore, simulations of n-C10 with the COMPASS force field have been conducted with three different integration schemes in advance. The three integration schemes are the standard velocity Verlet algorithm[2] with a time step of Δt = 0.25 fs and the RESPA multiple time step method[3] with a maximal time step of Δt = 1 fs and Δt = 2 fs. The results of these simulations are shown in Fig. S2. For all three properties (ρ, η, and D), the simulation results agree within their error bars. Based on this results, the RESPA integrator with a maximal time step of Δt = 2 fs was used for the all-atom force fields as the compuatational costs are reduced by more than a factor of 8 (Verlet) or 1.5 (RESPA with Δt = 1 fs).

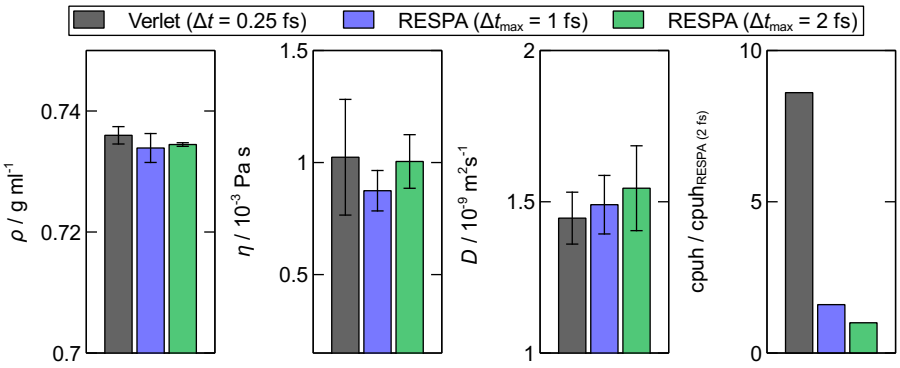

Figure S2. Density ρ, viscosity η, self-diffusion coefficient D, and the computational costs *cpuh* (from left to right) calculated from simulations of n-C10 with the COMPASS force field at p = 100 MPa and T = 373.15 K with three different integration schemes. Details on the different integration schemes are given in the text.

S3. LONG NPT RUN

To ensure equilibration in the NpT simulations, a long NpT simulation run of 100 ns was conducted (see Fig. S3). The total energy E_{tot} and the density ρ over time show that there

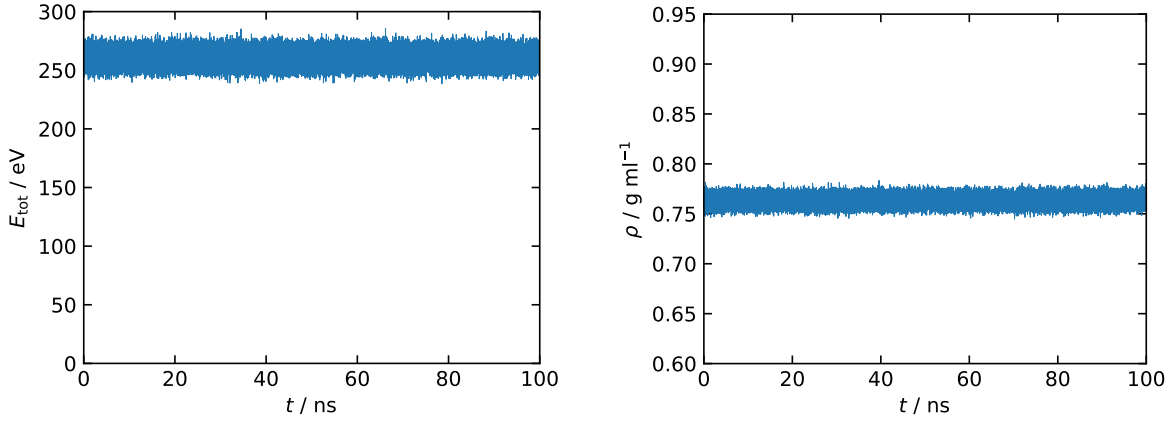

Figure S3. Total energy of the system E_{tot} and the density ρ as a function of the simulation time t for TRI with the Potoff force field at p = 0.1 MPa and T = 373.15 K.

is no shift. The equilibrated state is reached after few timesteps (t_{sim} < 1 ns).

S4. INFLUENCE OF THE CUTOFF CRITERION IN THE TDM

The cutoff criterion $\sigma(t_{\mathrm{cut}})/\eta(t_{\mathrm{cut}})$ of the time decomposition method was set to 0.4. It determines the time at which the autocorrelation function is cut to remove noise from the evaluation. To ensure a proper choice of the criterion, a series of 20 simulations of n-octane modeled by the TraPPE force field at ρ = 0.764 g ml^{-1} and T = 293 K was evaluated to caluclate the viscosity using cut criteria from 0.2 to 0.8. The results are shown in Fig. S4. The cutoff criterion does not have an influence on the simulation result. All results are

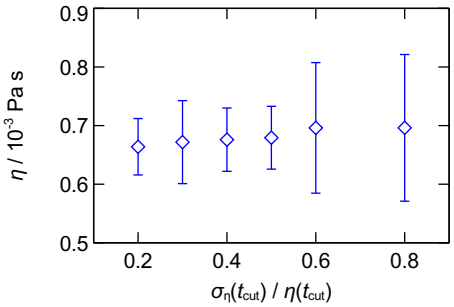

Figure S4. Viscosity η as function of the cutoff criterion $\sigma(t_{\mathrm{cut}})/\eta(t_{\mathrm{cut}})$ of the TDM for n-octane modeled by the TraPPE force field with ρ = 0.764 g ml^{-1} and T = 293 K.

within their error bars. For large values of $\sigma(t_{\mathrm{cut}})/\eta(t_{\mathrm{cut}})$ ($\geq$ 6), the calculated uncertainty increases.

S5. FORCE FIELD PARAMETERS

In the present section, the force fields that were used in the present work, are presented togehther with their paramaters. The following functions were used to describe the interaction potentials U:

$$U(r) = c\varepsilon\left[\left(\frac{\sigma}{r}\right)^n - \left(\frac{\sigma}{r}\right)^m\right] \quad \text{with} \quad c = \left(\frac{n}{n-m}\right)\left(\frac{n}{m}\right)^{\frac{m}{n-m}} \tag{S1}$$

$$U(r) = k_{\mathrm{b}}(r - r_0)^2 \tag{S2}$$

$$U(r) = k_2(r - r_0)^2 + k_3(r - r_0)^3 + k_4(r - r_0)^4 \tag{S3}$$

$$U(\theta) = k_\theta(\theta - \theta_0)^2 \tag{S4}$$

$$\begin{aligned} U(\theta) =& k_2(\theta - \theta_0)^2 + k_3(\theta - \theta_0)^3 + \\ & k_4(\theta - \theta_0)^4 + M(r_{ij} - r_1)(r_{jk} - r_2) + \\ & N_1(r_{ij} - r_1)(\theta - \theta_0) + N_2(r_{jk} - r_2)(\theta - \theta_0) \end{aligned} \tag{S5}$$

$$U(\phi) = k_0 + k_1(1 + \cos(\phi)) + k_2(1 + \sin(2\phi)) + k_3(1 + \cos(3\phi)) \tag{S6}$$

$$U(\phi) = 0.5k_1(1+\cos(\phi)) + 0.5k_2(1-\cos(2\phi)) + 0.5k_3(1+\cos(3\phi)) + 0.5k_4(1-\cos(4\phi)) \tag{S7}$$

$$\begin{aligned} U(\phi) =& \sum_{3}^{n=1} K_n(1 - cos(n\phi - \phi_n)) + \\ & (r_{jk} - r_2)(A_1 cos(\phi) + A_2 cos(2\phi) + A_3 cos(3\phi)) + \\ & (r_{ij} - r_1)(B_1 cos(\phi) + B_2 cos(2\phi) + B_3 cos(3\phi)) + \\ & (r_{kl} - r_3)(C_1 cos(\phi) + C_2 cos(2\phi) + C_3 cos(3\phi)) + \\ & (\theta_{ijk} - \theta_1)(D_1 cos(\phi) + D_2 cos(2\phi) + D_3 cos(3\phi)) + \\ & (\theta_{jkl} - \theta_2)(E_1 cos(\phi) + E_2 cos(2\phi) + E_3 cos(3\phi)) + \\ & M(\theta_{ijk} - \theta_1)(\theta_{jkl} - \theta_2) cos(\phi) \end{aligned} \tag{S8}$$

$$\begin{aligned} U(\phi) =& M_1(\theta_{ijk} - \theta_1)(\theta_{kjl} - \theta_2) cos(\phi) \\ & M_2(\theta_{ijk} - \theta_1)(\theta_{ijl} - \theta_2) cos(\phi) \\ & M_3(\theta_{ijl} - \theta_1)(\theta_{kjl} - \theta_2) cos(\phi) \end{aligned} \tag{S9}$$

UA force fields

The non-bonded parameters of the TraPPE, Potoff, and TAMie force field are given in Tab. S1 - S3. All three force fields use the same intramolecular parameters. The bond, angle, and dihedral interaction parameters are given in Tab. S4 - S6.

Table S1. Non-bonded interaction parameters of the TraPPE force field. Parameters given for the Lennard-Jones potential (see Eq. S1 with n = 12 and m = 6).

Site	ε /eV	σ /Å	Ref.
CH_3	0.008445	3.75	[4]
CH_2	0.003964	3.95	[4]
CH	0.000862	4.68	[5]

Table S2. Non-bonded interaction parameters of the Potoff force field. Parameters given for the Mie potential (see Eq. S1).

Site	n	m	ε /eV	σ /Å	Ref.
CH_3	16	6	0.010449	3.783	[6]
CH_2	16	6	0.005257	3.99	[6]
CH	16	6	0.001206	4.70	[7]

Table S3. Non-bonded interaction parameters of the TAMie force field. Parameters given for the Mie potential (see Eq. S1).

Site	n	m	ε /eV	σ /Å	Ref.
CH_3	14	6	0.011747	3.60	[8]
CH_2	14	6	0.004560	4.04	[8]
CH	14	6	0.001253	4.37	[9]

Table S4. Bond interaction parameters of the UA force fields. Parameters given for the harmonic potential (see Eq. S2).

Bond	k_b /eVÅ^{-1}	r_0 /Å	Ref.
CH_x-CH_y	11.6216	1.54	[4,10]
CH_3-CH_y (only TAMie)	11.6216	1.74	[8,10]

Table S5. Angle interaction parameters of the UA force fields. Parameters given for the harmonic potential (see Eq. S4).

Angle	k_θ /eV	θ_0 /°	Ref.
CH_x-CH_2-CH_y	2.6929	114	[4]
CH_x-CH-CH_y	2.6929	112	[5]

Table S6. Dihedral interaction parameters of the TraPPE force field. Parameters given for the Fourier potential (see Eq. S6).

Dihedral	k_0 /eV	k_1 /eV	k_2 /eV	k_3 /eV	Ref.
CH_x-CH_2-CH_2-CH_y	0	0.03059	-0.00588	0.06819	[4]
CH_x-CH_2-CH-CH_y	-0.02163	0.03695	-0.00964	0.03803	[5]

OPLS

The non-bonded parameters of the OPLS force field are given in Tab. S7. The bond, angle, and dihedral interaction parameters are given in Tab. S8 - S10.

Table S7. Non-bonded interaction parameters an charges of the OPLS force field. Parameters given for the Lennard-Jones potential (see Eq. S1 with n = 12 and m = 6).

Site	ε /eV	σ /Å	q /e	Ref.
C (CH_3)	0.002862	3.5	-0.18	[11]
C (CH_2)	0.002862	3.5	-0.12	[11]
C (CH)	0.002862	3.5	-0.06	[11]
H	0.001301	2.5	0.06	[11]

Table S8. Bond interaction parameters of the OPLS force field. Parameters given for the harmonic potential (see Eq. S2).

Bond	k_b /eVÅ^{-1}	r_0 /Å	Ref.
C-C	11.6216	1.529	[11]
C-H	14.7438	1.090	[11]

Table S9. Angle interaction parameters of the OPLS force field. Parameters given for the harmonic potential (see Eq. S4).

Angle	k_θ /eV	θ_0 /°	Ref.
C-C-C	2.5303	112.7	[11]
C-C-H	1.6262	110.7	[11]
H-C-H	1.4310	107.8	[11]

Table S10. Dihedral interaction parameters of the OPLS force field. Parameters given for the OPLS potential (see Eq. S7).

Dihedral	k_1 /eV	k_2 /eV	k_3 /eV	Ref.
C-C-C-C	0.07545	-0.00681	0.01210	[11]
C-C-C-H	0.0	0.0	0.01587	[11]
H-C-C-H	0.0	0.0	0.01379	[11]

L-OPLS

The non-bonded parameters of the L-OPLS force field are given in Tab. S11. The C-C bond potential of the L-OPLS is given in Tab. S8. The C-H is rigid with a distance of r_0 = 1.09 Å. The angle interaction parameters of the L-OPLS force field are the same as those of the OPLS force field (see Tab. S9). The dihedral parameter are given in Tab. S12.

Table S11. Non-bonded interaction parameters an charges of the L-OPLS force field. Parameters given for the Lennard-Jones potential (see Eq. S1 with n = 12 and m = 6).

Site	ε /eV	σ /Å	q /e	Ref.
C (CH_3)	0.002862	3.5	-0.222	[12]
C (CH_2)	0.002862	3.5	-0.148	[12]
C (CH)	0.002862	3.5	-0.06	[12]
H (CH_3)	0.001301	2.5	0.074	[12]
H (CH_2)	0.001140	2.5	0.074	[12]
H (CH)	0.001301	2.5	0.06	[12]

Table S12. Dihedral interaction parameters of the L-OPLS force field. Parameters given for the OPLS potential (see Eq. S7).

Dihedral	k_1 /eV	k_2 /eV	k_3 /eV	Ref.
C-C-C-C	0.02796	-0.00929	0.00773	[12]
C-C-C-H	0.0	0.0	0.01301	[13]
H-C-C-H	0.0	0.0	0.01301	[13]

COMPASS

The parameters for the non-bonded (cf. Tab. S13), the bond (cf. Tab. S14) the angle (cf. Tab. S15), the dihedral (cf. Tab. S16), and the improper (cf. Tab. S17) interactions are given in the following.

Table S13. Non-bonded interaction parameters and charges of the COMPASS force field. Parameters given for the Mie potential (see Eq. S1) with n = 9 and m = 6.

Site	ε /eV	σ /Å	q /e	Ref.
C (CH_3)	0.002689	3.8540	-0.159	[14]
C (CH_2)	0.002689	3.8540	-0.106	[14]
C (CH)	0.001735	3.8540	-0.053	[14]
H	0.000997	2.8780	0.053	[14]

Table S14. Bond interaction parameters of the COMPASS force field. Parameters given for the quartic potential (see Eq. S3).

Bond	k_2 /eVÅ^{-2}	k_3 /eVÅ^{-3}	k_4 /eVÅ^{-4}	r_0 /Å	Ref.
C-C	12.9949	-21.7588	29.4794	1.530	[14]
C-H	14.9606	-30.0032	36.6253	1.101	[14]

Table S15. Angle (3-body) interaction parameters of the COMPASS force field. Parameters given for the potential given by Eq. S5. The equilibrium bonds r_1 and r_2 are given in Tab. S14.

Angle $(i-j-k)$	k_2 /eV	k_3 /eV	k_3 /eV	θ_0 /°	M /eV	N_1 /eV	N_2 /eV	Ref.
C-C-C	1.7136	-0.3228	-0.4145	112.67	0.0	0.3476	0.3476	[14]
C-C-H	1.7976	-0.4598	0.2224	110.77	0.1469	0.9000	0.4953	[14]
H-C-H	1.7190	-0.5603	-0.1055	107.66	0.2312	0.7850	0.7850	[14]

Table S16. Dihedral (4-body) interaction parameters of the COMPASS force field. Parameters given for the potential given by Eq. S8. The equilibrium bonds $r_1 - r_3$ as well as the equilibrium angles $\theta_1 - \theta_2$ are given in Tab. S14 and S15.

Dihedral $(i-j-k-l)$	K_1 /eV	K_2 /eV	K_3 /eV	A_1 /eVÅ^{-1}	A_2 /eVÅ^{-1}	A_3 /eVÅ^{-1}	Ref.
C-C-C-C	0.0	0.0022	-0.0062	-0.7713	-0.3117	0.0	[14]
C-C-C-H	0.0	0.0014	-0.0073	-0.6452	-0.1586	-0.0136	[14]
H-C-C-H	-0.0062	0.0027	-0.0066	-0.6184	-0.0231	-0.0211	[14]
	B_1 /eVÅ^{-1}	B_2 /eVÅ^{-1}	B_3 /eVÅ^{-1}	C_1 /eVÅ^{-1}	C_2 /eVÅ^{-1}	C_3 /eVÅ^{-1}	
C-C-C-C	-0.0032	0.0	0.0	-0.0032	0.0	0.0	[14]
C-C-C-H	0.0108	0.0105	-0.0040	0.0035	0.0026	0.0096	[14]
H-C-C-H	0.0092	0.0135	0.0034	0.0092	0.0135	0.0034	[14]
	D_1 /eV	D_2 /eV	D_3 /eV	E_1 /eV	E_2 /eV	E_3 /eV	
C-C-C-C	0.0169	-0.0136	0.0060	0.0169	-0.0136	0.0060	[14]
C-C-C-H	-0.0106	0.0	-0.0049	0.0135	0.0196	-0.0086	[14]
H-C-C-H	-0.0351	0.0242	-0.0107	-0.0351	0.0242	-0.0107	[14]
	M /eV						
C-C-C-C	-0.9560						[14]
C-C-C-H	-0.7009						[14]
H-C-C-H	-0.5448						[14]

Table S17. Improper (4-body) interaction parameters of the COMPASS force field. Parameters given for the potential given by Eq. S9. The equilibrium angles $\theta_1 - \theta_3$ are given in Tab. S15. The atom j defines the central atom of the improper.

Improper $(i-j-k-l)$	M_1 /eV	M_2 /eV	M_3 /eV	Ref.
C-C-C-C	-0.0075	-0.0075	-0.0075	[14]
C-C-C-H	-0.0572	-0.0572	0.0051	[14]
H-C-C-H	0.0119	-0.0209	0.0119	[14]
H-C-H-H	-0.0137	-0.0137	-0.0137	[14]

MARTINI

The coarse-grained models of all five substances as used in this work are shown in Fig. S5.

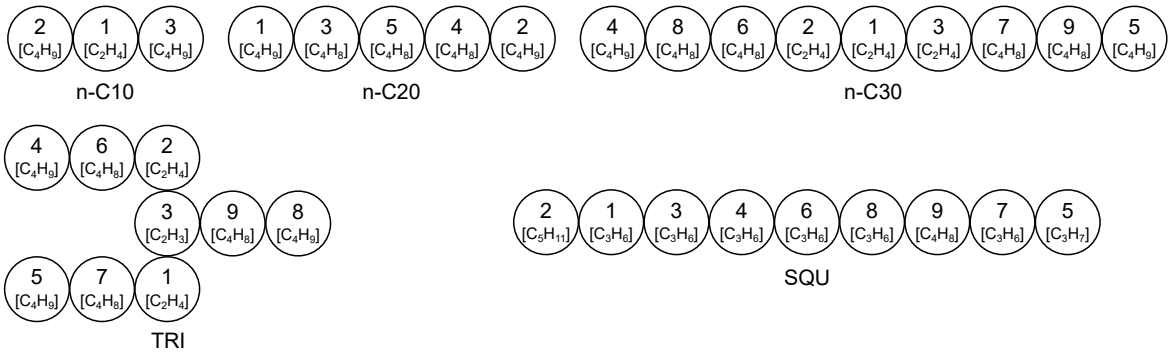

Figure S5. Coarse grained models for the Martini force field used in this work.

The parameters for the non-bonded, the bond, and the angel interaction potentials are given in Tab. S18 – S20.

Table S18. Non-bonded interaction parameters of the MARTINI force field as used in this work. Parameters given for the Lennard-Jones potential (see Eq. S1 with n = 12 and m = 6).

Molecule	Interaction sites	ε /eV	σ /Å
n-C10, n-C20, n-C30, TRI	C_2H_4 – C_2H_4	0.0363	4.7
	C_4H_x – C_4H_y	0.0321	4.7
	C_2H_4 – C_4H_y	0.0363	4.7
SQU	C_xH_y – C_xH_y	0.0363	4.7

Table S19. Bond interaction parameters of the MARTINI force field as used in this work. Parameters given for the harmonic bond potentials (see Eq. S2).

Molecule	Bond	k_b /eVÅ^{-1}	r_0 /Å
n-C10	1 – 2	0.0648	3.390
	1 – 3	0.0648	3.410
n-C20	1 – 3	0.0648	4.942
	2 – 4	0.0648	4.930
	3 – 5	0.0648	5.001
	4 – 5	0.0648	4.977
n-C30	1 – 2	0.0648	3.291
	1 – 3	0.0648	3.291
	2 – 6	0.0648	4.452
	3 – 7	0.0648	4.425
	4 – 8	0.0648	5.600
	5 – 9	0.0648	5.667
	6 – 8	0.0648	5.667
	7 – 9	0.0648	5.654
TRI	1 – 3	0.0648	3.290
	1 – 7	0.0648	4.420
	2 – 3	0.0648	3.348
	2 – 6	0.0648	4.608
	3 – 9	0.0648	4.608
	4 – 6	0.0648	5.782
	5 – 7	0.0648	5.869
	8 – 9	0.0648	5.884
SQU	1 – 2	0.0648	3.290
	1 – 3	0.0648	4.420
	3 – 4	0.0648	3.348
	4 – 6	0.0648	4.608
	5 – 7	0.0648	4.608
	6 – 8	0.0648	5.782
	7 – 9	0.0648	5.869
	8 – 9	0.0648	5.884

Table S20. Angle interaction parameters of the MARTINI force field as used in this work. Parameters given for the harmonic angle potentials (see Eq. S4).

Molecule	Bond	k_θ /eV	θ_0 /°
n-C10	2 – 1 – 3	0.1296	143.1
n-C20	1 – 3 – 5	0.1296	142.5
	2 – 4 – 5	0.1296	142.4
	3 – 5 – 4	0.1296	143.6
n-C30	2 – 1 – 3	0.1296	137.1
	1 – 2 – 6	0.1296	131.4
	1 – 3 – 7	0.1296	130.7
	2 – 6 – 8	0.1296	137.5
	3 – 7 – 9	0.1296	139.7
	4 – 8 – 6	0.1296	137.7
	5 – 9 – 7	0.1296	136.8
TRI	3 – 1 – 7	0.1296	102.4
	1 – 3 – 2	0.1296	117.5
	1 – 3 – 9	0.1296	119.1
	1 – 7 – 5	0.1296	132.8
	3 – 2 – 6	0.1296	136.0
	2 – 3 – 9	0.1296	87.8
	2 – 6 – 4	0.1296	138.8
	3 – 9 – 8	0.1296	137.5
SQU	2 – 1 – 3	0.1296	119.3
	1 – 3 – 4	0.1296	138.7
	3 – 4 – 6	0.1296	120.3
	4 – 6 – 8	0.1296	135.4
	5 – 7 – 9	0.1296	140.8
	6 – 8 – 9	0.1296	126.1
	7 – 9 – 8	0.1296	126.9

Reactive force fields

For both reactive force fields, external input files have been used. The *CHON-2017_weak* version of the ReaxFF is provided in the Supplementary Material of Ref.[15]. For the AIREBO-M, the file distributed by LAMMPS (Version 3 March 2020) was used (*CH.airebo-m*).

S6. VALIDATION

In the following, the implementation of some force fields as used in this work is validated using literature data. As can be seen in Fig. S6 - S10, the results agree well with the values

given in the literature.

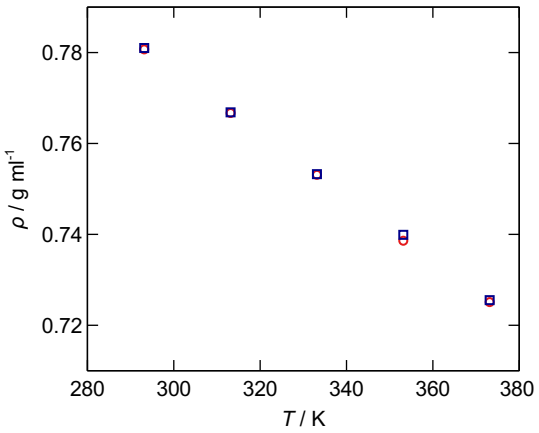

Figure S6. Validation of the ReaxFF force field with data from *Morrow and Harrison*[16] for the density ρ of n-hexadecane as function of temperature T at a pressure p = 0.1 MPa. Blue squares represent the result from this work and red circles the results from literature.

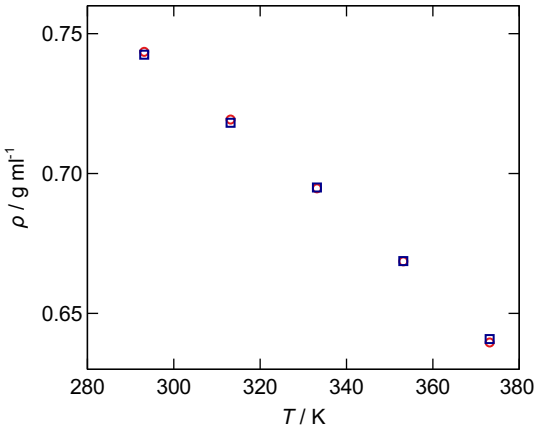

Figure S7. Validation of the AIREBO-M force field with data from *Morrow and Harrison*[16] for the density ρ of n-hexadecane as function of temperature T at a pressure p = 0.1 MPa. Blue squares represent the result from this work and red circles the results from literature.

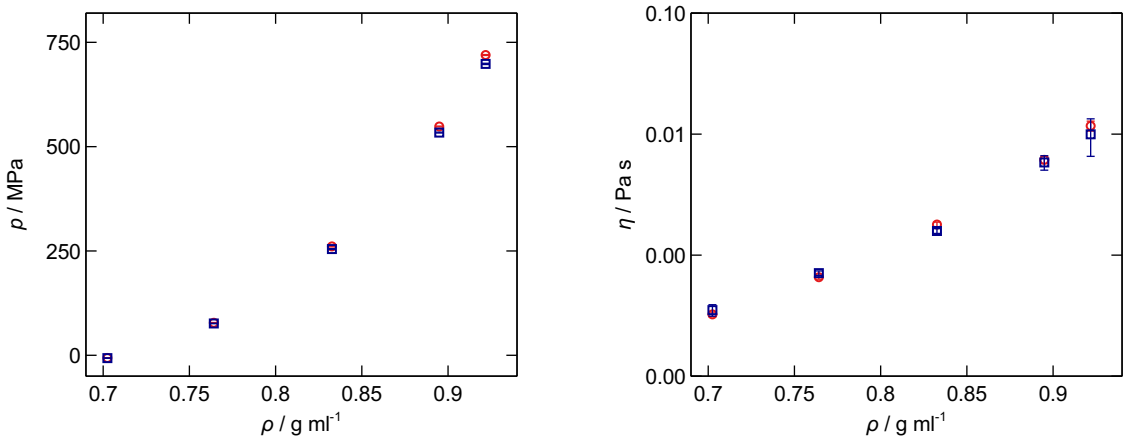

Figure S8. Validation of the TraPPE force field with data from *Messerly et al.*[17] for the pressure p and the viscosity η of n-octane as function of density ρ at a temperature T = 293 K. Blue squares represent the result from this work and red circles the results from literature.

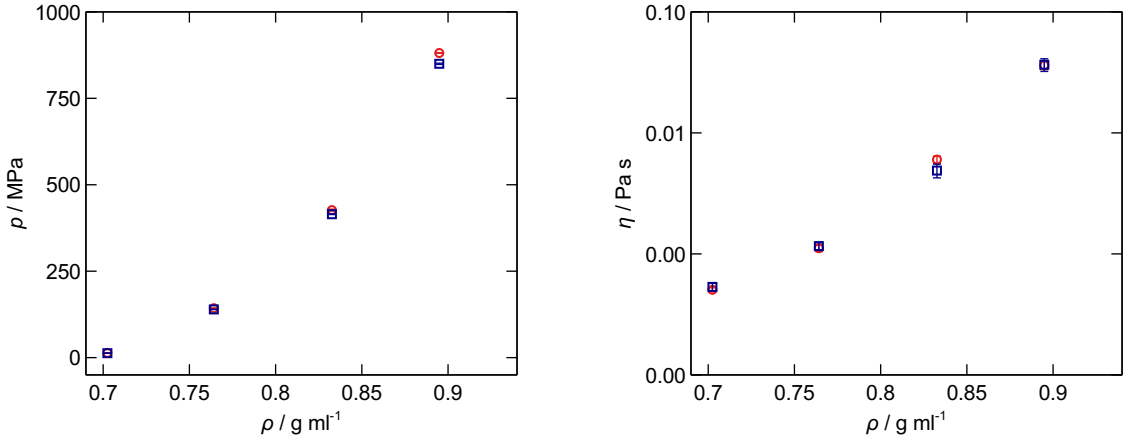

Figure S9. Validation of the TAMie force field with data from *Messerly et al.*[17] for the pressure p and the viscosity η of n-octane as function of density ρ at a temperature T = 293 K. Blue squares represent the result from this work and red circles the results from literature.

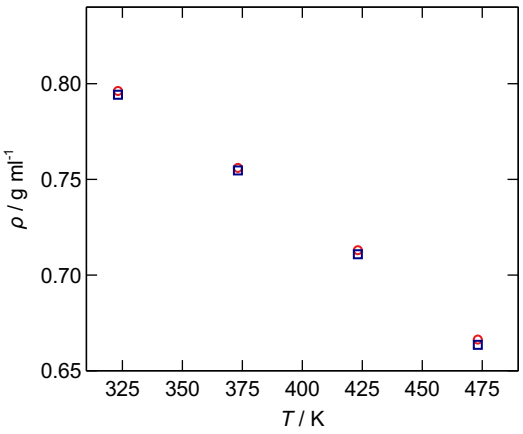

Figure S10. Validation of the MARTINI force field with data from *Papavasileiou et al.*[18] for the density ρ of n-dodecane as function of temperature T at a pressure p = 0.1 MPa. Blue squares represent the result from this work and red circles the results from literature.

S7. CORRELATIONS OF EXPERIMENTAL DATA

Equation S10 was used to fit the experimental data.

$$y/[y] = \frac{a_0 + a_1(T/\mathrm{K}) + a_2(p/\mathrm{MPa}) + a_3(p/\mathrm{MPa})^2 + a_4(T/\mathrm{K})(p/\mathrm{MPa})}{1 + b_1(T/\mathrm{K}) + b_2(p/\mathrm{MPa}) + b_3(T/\mathrm{K})(p/\mathrm{MPa})} \tag{S10}$$

Table S21 shows the units of the properties used for the fits with Equation S10.

Table S21. Units of the correlations used with Equation S10.

y	$[y]$
ρ	g/ml
η	Pa s
D	m^2/s
λ	W/(K m)

The references of the experimental data are given in the main text. Table S22 contains the fitted parameters as well as the AAD of the fits for all properties with experimental data available.

Table S22. Correlation parameters for equation S10.

substance	property	a_0	a_1	a_2	a_3	a_4	b_1	b_2	b_3	AAD / %
n-C10	ρ	9.44e−1	−8.35e−4	3.43e−3	1.11e−6	6.23e−6	−1.43e−4	3.52e−3	9.16e−6	0.13
	$\log(\eta)$	8.64e1	−8.17e−1	1.57e0	1.03e−3	−8.56e−3	7.14e−2	−1.23e−1	1.0e−3	1.4
	$\log(D)$	−4.51e1	−2.43e−1	1.52e−1	−6.65e−5	−2.23e−3	1.60e−2	−140e−2	1.22e−4	1.61
n-C20	ρ	9.57e−1	−8.23e−4	4.64e−3	1.38e−6	4.47e−6	−3.13e−4	5.04e−3	6.35e−6	0.16
	$\log(\eta)$	1.05e1	−9.09e−2	2.49e−1	7.36e−5	−8.84e−4	6.94e−3	−2.01e−2	1.07e−4	0.43
n-C30	ρ	9.64e−1	−7.42e−4	5.66e−3	1.41e−6	2.58e−6	−2.51e−4	6.13e−3	4.13e−6	0.13
	$\log(D)$	−1.64e7	−1.17e5	6.00e4	−2.67e1	−7.67e2	7.42e3	−5.82e3	3.98e1	1.22
TRI	$\log(\eta)$	1.82e7	−8.32e4	1.44e5	4.59e1	−4.49e2	5.87e3	−9.9e3	5.38e1	3.19
SQU	ρ	9.96e−1	−7.03e−4	5.46e−4	2.55e−7	8.42e−6	−7.82e−5	1.52e−4	9.88e−6	0.28
	$\log(\eta)$	2.65e7	−1.18e5	2.37e5	8.14e1	−7.05e2	8.11e3	−1.4e4	7.44e1	5.12

S8. CORRELATIONS OF SIMULATION DATA

The parameters for the properties without experimental data available are given in Table S23.

Table S23. Correlation parameters for equation S10 with $a_1 = 0$, $a_4 = 0$, $b_1 = 0$, and $b_3 = 0$.

substance	property	a_0	a_2	a_3	b_2	AAD / %
n-C20	$\log(D)$	−2.09e1	−8.06e−3	4.77e−6	6.19e−16	0.07
n-C30	$\log(\eta)$	−5.86e0	7.22e−3	−3.64e−6	1.01e−15	0.34
TRI	ρ	7.64e−1	4.36e−3	5.33e−7	4.75e−3	0.01
	$\log(D)$	−2.22e1	−1.76e−1	−4.57e−5	7.23e−3	0.03
SQU	$\log(D)$	−2.22e1	−2.03e−2	4.68e−6	3.31e−4	0.02

They were fitted to the simulation results of the Potoff force field.

S9. ELECTRONIC SUPPLEMENTARY MATERIAL OF THE NUMERIC DATA

The simulation results are given in the electronic Supplementary Material as additional *xlsx* files. The data comprise the temperature `T`, the density `rho`, the pressure `p`, the viscosity `eta`, and the self-diffusion coefficient `D` as calculated from the NVT simulations. The uncertainties, calculated as described in the main part, are also given as `dT`, `drho`, `dp`, `deta`, and `dD`, respectively. The units are the same as in the Fig. 6, 8, and 10 of the main part of this paper.

S10. RADIUS OF GYRATION

The radius of gyration was calculated for all simulations. The results are shown in Fig. S11 for all molecules and force fields. There is only a weak pressure dependency of R_g. Especially the simulations with the MARTINI force field show a decrease of the radius of gyration with increasing pressure. The strong decrease of R_g for pressures $p > 50$ MPa observed by Prentice et al.[19] for SQU with the L-OPLS force field could not be confirmed. The radius of gyration was averaged over all pressures for every force field and molecule. The results are shown in Fig. S12. The radius of gyration increases with increasing chainlength for the linear alkanes as expected. The two branched alkanes show lower radii of gyration compraed ot their isomer n-C30. TRI (long branches) exhibits thereby smaller radius of gyration then SQU (short branches). The different force fields show very similar results for the radius of gyration. Only the simulations with the OPLS force field for n-C20 and n-C30 and the MARTINI force field for SQU deviate from the other force fiels. For OPLS,

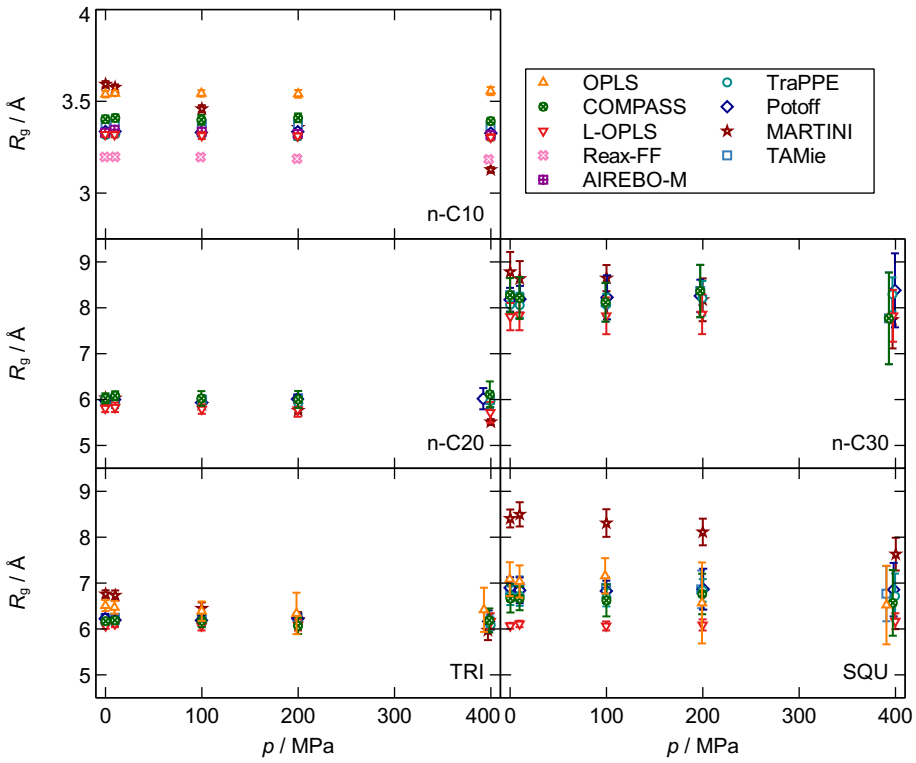

Figure S11. Radius of gyration R_g of n-C10, n-C20, n-C30, TRI, and SQU at T = 373.15 K as a function of the pressure p. Colored symbols indicate the simulation results for the different force fields.

this is already known as its results for long linear alkanes show unphysical behavio (see Section S11). The deviation of the MARTINI force field for SQU can be explained by the representation by MARTINI as a linear chain (see Section S5).

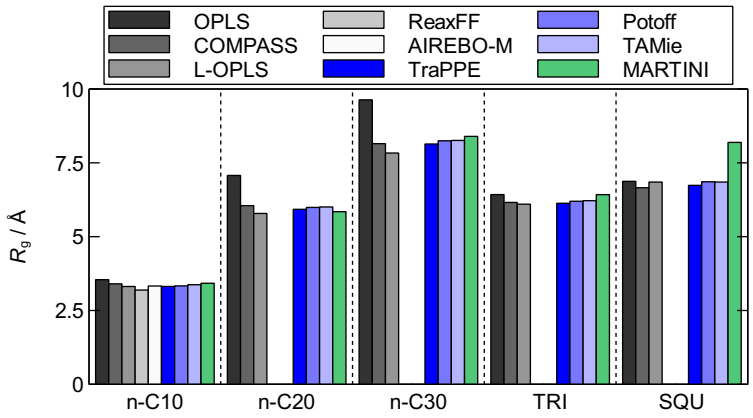

Figure S12. Averaged radius of gyration R_g of n-C10, n-C20, n-C30, TRI, and SQU at T = 373.15 K for the different force fields averaged over all state points.

S11. OPLS SIMULATIONS OF N-ICOSANE AND N-TRIACONTANE

The simulations for n-icosane (n-C20) and n-triacontane (n-C30) with the OPLS force field exhibit an unphysical transition to a gel-like phase, which has already been described by Ref.[12]. Therefore, these simulations were discarded in the main part. For transparency, these results are shown here in the Supplementary Material. A screenshot of such a gel-like phase of n-icosane (n-C20) at a density of 0.833 g/ml is shown in Fig. S13.

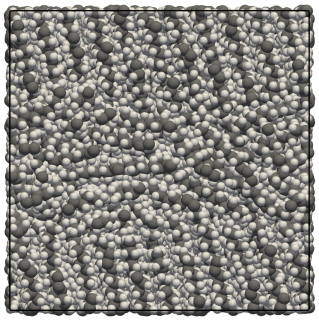

Figure S13. Screenshot of an NVT simulation of n-icosane (n-C20) at ρ = 0.833 g/ml and T = 373.15 K. The single sites are colored as follows: gray - carbon, white - hydrogen.

The backbones of the n-icosane (n-C20) molecules are blockwise structured in parallel. In measurements, the phase transition to solid-like phase is observed at significantly lower temperatures than considered in this work[12]. In general, the single replica simulations

exhibit different metastable states and are inhomogeneous. The transition to the gel-like phase strongly influences the prediction of the density and leads to high uncertainties of the pressure in the NVT simulations due to different degrees of structuring in the set of replica simulations. Additionally the densities calculated from the preliminary NpT simulations do not reproduce the pressure in the NVT simulations which is why the OPLS simulations do not match the prescribed pressures. This structuring can only be observed for n-icosane (n-C20) and n-triacontane (n-C30) modeled by the OPLS force field.

The results for the densities of n-C20 and n-C30 calculated with the OPLS force field are shown in Fig. S14. For both substances, the simulations show large deviations to the

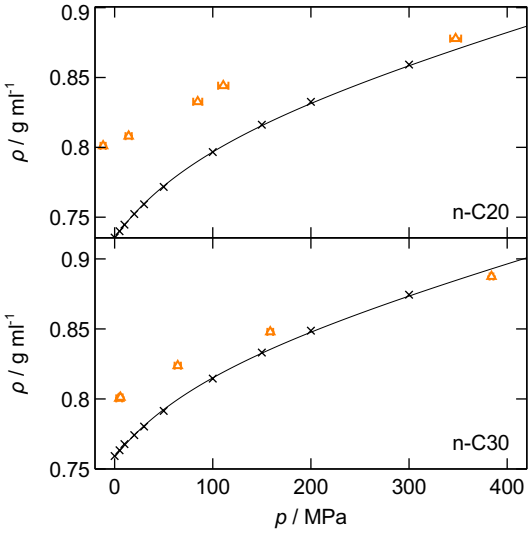

Figure S14. Density ρ as function of pressure p for n-C20 and n-C30. Symbols indicate the simulation results for the OPLS force field. Lines represent the empirical correlations (black solid lines in cases where exp. data was used). All properties given for the temperature T = 373.15 K.

experimental data. Except for the highest pressure, the densities are strongly overestimated.

In Fig. S15, the viscosity results for n-C20 and n-C30 simulated with the OPLS force field are displayed. For nearly all state points, the OPLS force fields overestimated the experimental data by more than one order of magnitude. The increased viscosity is a result of the decreased mobility of the molecules due to the structuring.

The results for the self-diffusion coefficient of n-C20 and n-C30 of the OPLS force field are shown in Fig. S16. As expected from the increased viscosity, the OPLS force field underestimates the experimental data.

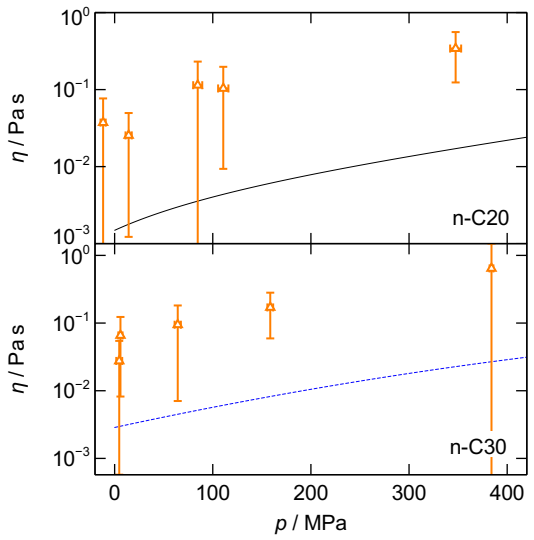

Figure S15. Viscosity η as function of pressure p for n-C20 and n-C30. Symbols indicate the simulation results for the OPLS force field. Lines represent the empirical correlations (black solid lines in cases where exp. data was used; blue dotted lines in cases where the Potoff force field was used). All properties given for the temperature T = 373.15 K.

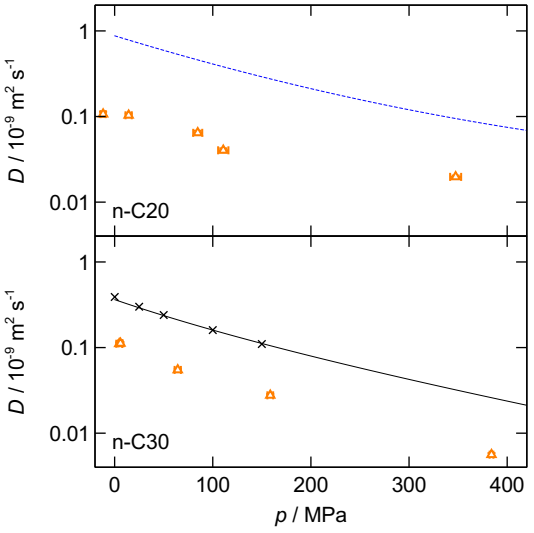

Figure S16. Self-diffusion coefficient D as function of pressure p for n-C20 and n-C30. Symbols indicate the simulation results for the OPLS force field. Lines represent the empirical correlations (black solid lines in cases where exp. data was used; blue dotted lines in cases where the Potoff force field was used). All properties given for the temperature T = 373.15 K.

S12. RELATION BETWEEN VISCOSITY AND SELF-DIFFUSION

Fig. S17 shows the linear relation between the self-diffusion coefficient and the viscosity as predicted by the Stokes-Einstein relation[20]. Using the Stokes-Einstein equation (see Eq.

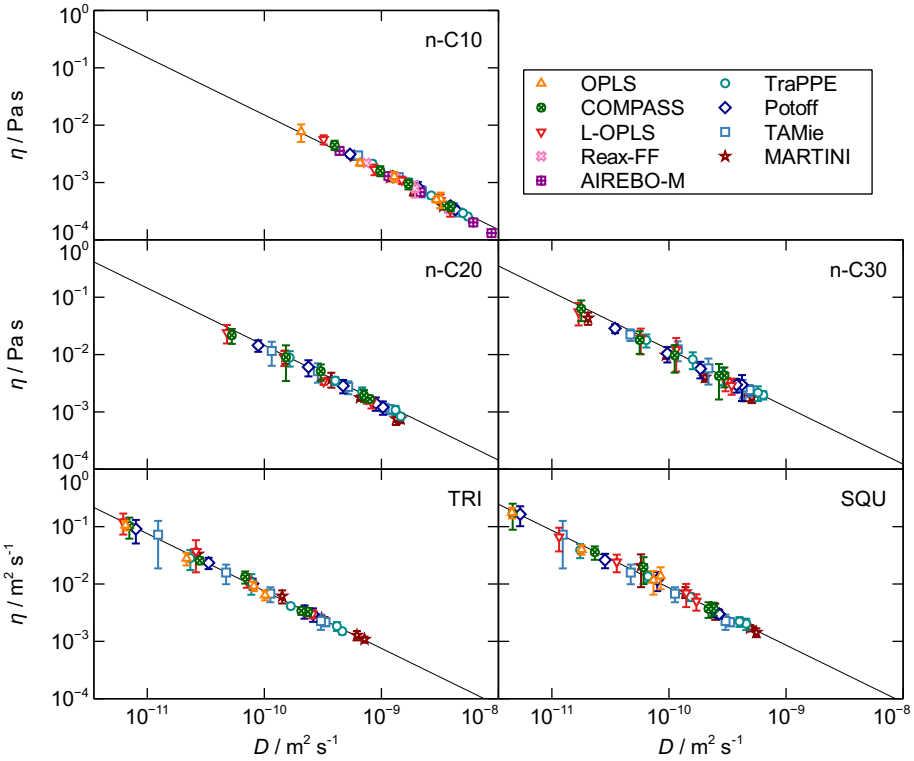

Figure S17. Viscosity η as function of the self-diffusion coefficient D for n-C10, n-C20, n-C30, TRI, and SQU. Symbols indicate the simulation results for the different force fields. All properties given for the temperature T = 373.15 K and pressures p = 0.1 − 400 MPa.

S11), the hydrodynamic radii r_h were calculated for each state point.

$$D = \frac{k_\mathrm{B} T}{6\pi\eta r_\mathrm{h}} \tag{S11}$$

The results are given in Fig. S18. A dependency of the hydrodynamic radius R_h on the pressure is hardly detectable. Thus, a breakdown of the Stokes-Einstein relation for high pressure as observed by Ref.[19] is not found. However, the values for the hydrodynamic radius of SQU are in accordance with the vallues given by Prentice et al. for low pressure (p < 50 MPa).

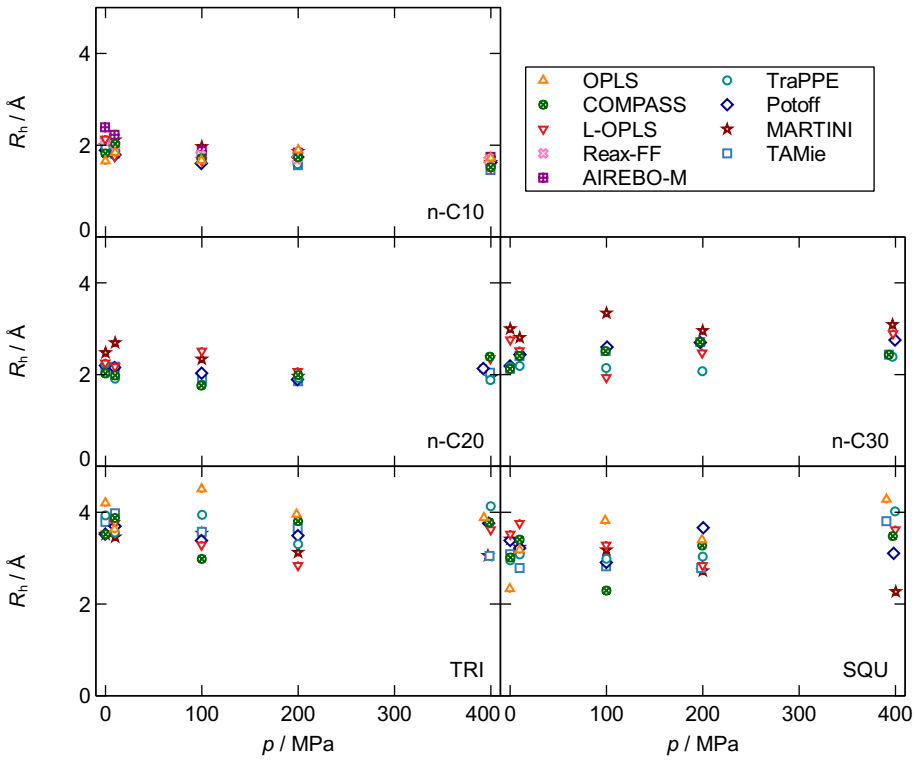

Figure S18. Hydrodynamic radius R_h of n-C10, n-C20, n-C30, TRI, and SQU at T = 373.15 K as a function of the pressure p. Colored symbols indicate the simulation results for the different force fields.

The hydrodynamic radius was also averaged over all pressures for every force field and molecule. The results are shown in Fig. S19.

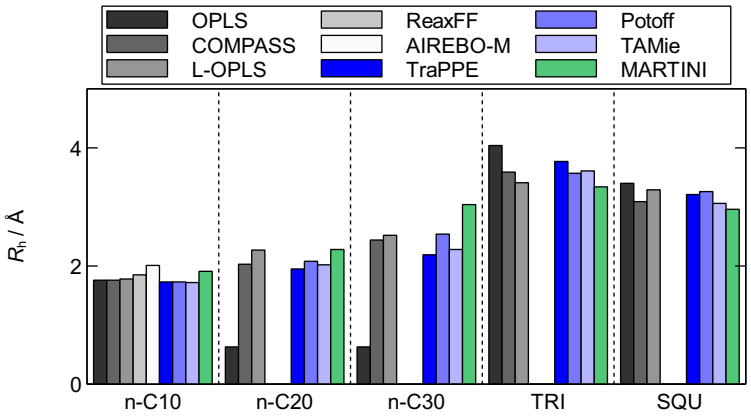

Figure S19. Averaged radius of gyration R_h of n-C10, n-C20, n-C30, TRI, and SQU at T = 373.15 K for the different force fields averaged over all state points.

The results are similar to the radius of gyration (see Fig. S12). The force fields are mostly consistent in their prediction of the hydrodynamic radius except the OPLS force field for n-C20 and n-C30. Due to its unphysical properties for long linear alkanes, it predicts smaller values than all other force fields. In general, the hydrodynamic radius is smaller than the radius of gyration which is in accordance with Ref.[19].

S13. RESULTS FOR THE MARTINI FORCE FIELD WITH TIME SCALING

In Fig. S20 and S21, the results for the viscosity and the self-diffusion coefficient calculated by the MARTINI force field with time scaling are compared to the original MARTINI results without time scaling. For the time scaling, a scaling factor $k_\mathrm{t} = 4$ was applied. The viscosity and the self-diffusion coefficient with time scaling were calculated from the original values of the MARTINI force field by $\eta_\mathrm{scaled} = \eta \cdot k_\mathrm{t}$ and $D_\mathrm{scaled} = D/k_\mathrm{t}$, respectively. For both properties, the predictions by the MARTINI force field worsen for the linear alkanes. They overestimate the viscosity and underestimate the self-diffusion clearly for all three substances where the original MARTINI without time scaling provided good predictions. In contrast, the predictions for the branched alkanes improve: The viscosity is underestimated and the self-diffusion is overestimated without time scaling. With time scaling, the deviations to the experimental values decrease. Overall, the time scaling does not improve the results throughout all substances and state points. Additionally, the factor itself is kind of arbitrary. For example, the standard scaling factor $k_\mathrm{t} = 4$ was derived from the comparison of the diffusional dynamics of water in CG simulations and experiments. Higher scaling factors (5-10) have been also used for different systems[21].

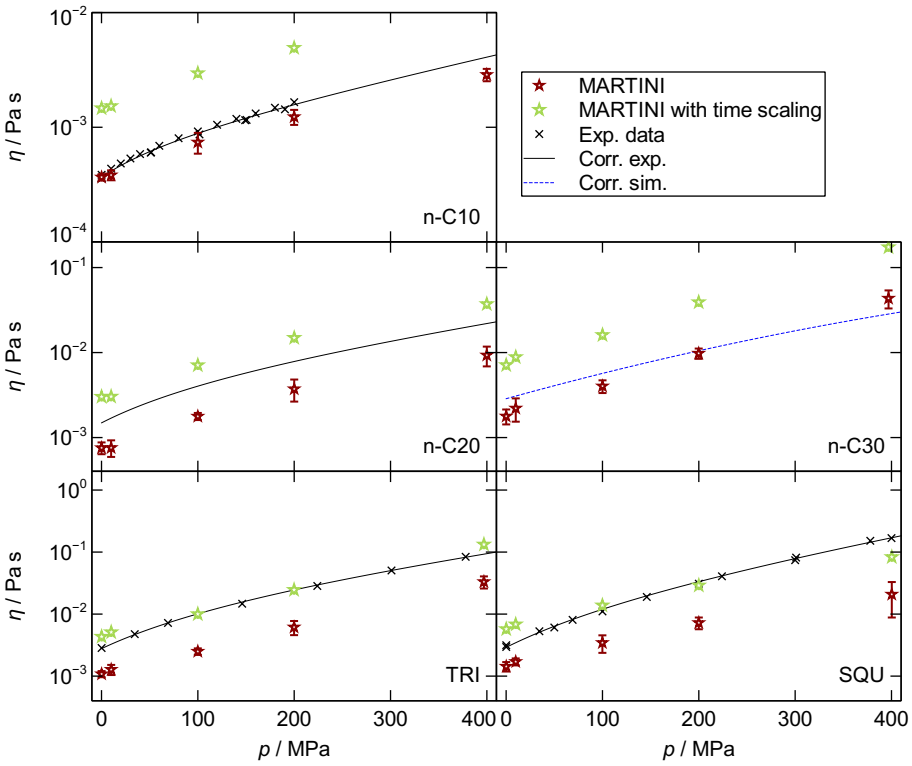

Figure S20. Viscosity η of n-C10, n-C20, n-C30, TRI, and SQU at T = 373.15 K as a function of the pressure p. Stars indicate the simulation results for the MARTINI force field without (dark red) and with scaling (light green) and the black crosses are experimental data points. Black solid lines are correlations of the experimental data, blue broken lines are correlations of the simulation data with the Potoff force field.

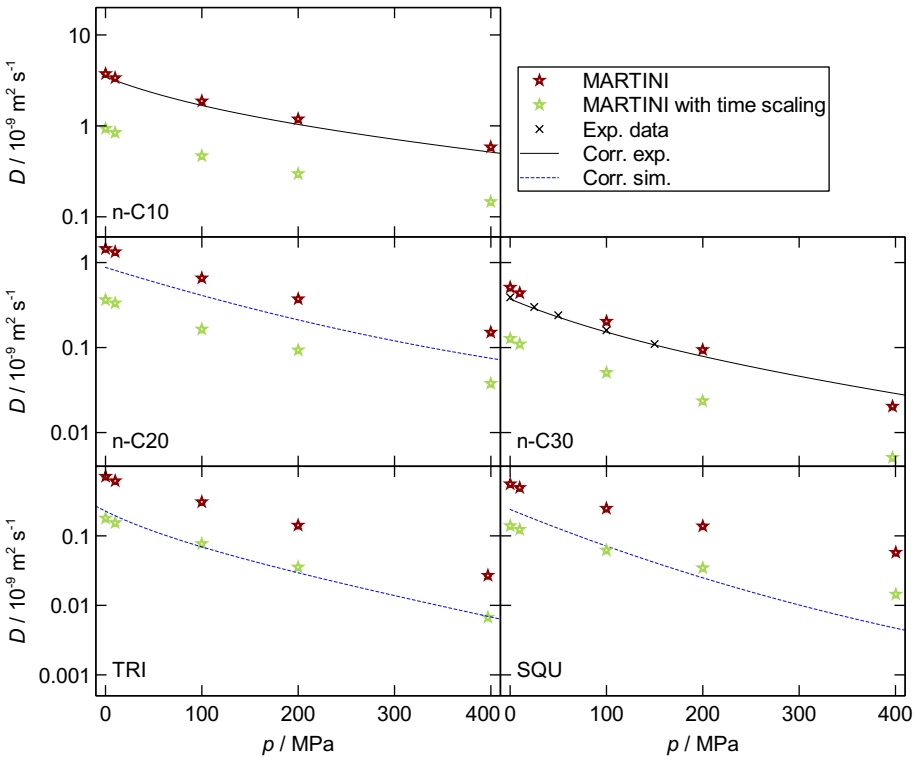

Figure S21. Self-Diffusion D of n-C10, n-C20, n-C30, TRI, and SQU at T = 373.15 K as a function of the pressure p. Stars indicate the simulation results for the MARTINI force field without (dark red) and with scaling (light green) and the black crosses are experimental data points. Black solid lines are correlations of the experimental data, blue broken lines are correlations of the simulation data with the Potoff force field.

S14. UNCERTAINTIES OF THE SIMULATIONS FOR THE COMPUTATIONAL COSTS

The uncertainties shown in Fig. S22 give an impression of the statistical quality of the simulations that were compared by their computational costs. For the viscosity, $\Delta\eta$ is between 7.4 % and 22 % of the computed value. The uncertainty of the self-diffusion coefficient is smaller in the range between 1 % and 1.6 %. For both properties, the uncertainties of the AA force fields tends to be slightly larger then the uncertainties of the UA and CG force fields. For the self-diffusion, this trend is even more mitigated.

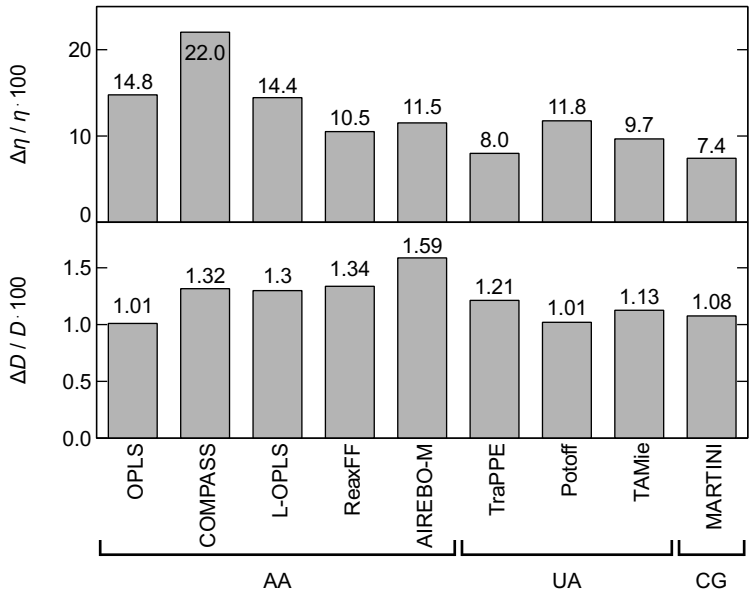

Figure S22. Uncertainties of the viscosity $\Delta\eta$ and the self-diffusion coefficient ΔD of all force fields for 20 replica simulations with T = 373.15 K and ρ = 0.67982 g/ml..

REFERENCES

[1] I.-C. Yeh and G. Hummer, "System-Size Dependence of Diffusion Coefficients and Viscosities from Molecular Dynamics Simulations with Periodic Boundary Conditions," The Journal of Physical Chemistry B **108**, 15873–15879 (2004).

[2] M. P. Allen and D. J. Tildesley, *Computer Simulation of Liquids*, 2nd ed. (Oxford University Press, Oxford, United Kingdom, 2017).

[3]M. Tuckerman, B. J. Berne, and G. J. Martyna, "Reversible multiple time scale molecular dynamics," The Journal of Chemical Physics **97**, 1990–2001 (1992).

[4]M. G. Martin and J. I. Siepmann, "Transferable Potentials for Phase Equilibria. 1. United-Atom Description of n-Alkanes," The Journal of Physical Chemistry B **102**, 2569–2577 (1998).

[5]M. G. Martin and J. I. Siepmann, "Novel Configurational-Bias Monte Carlo Method for Branched Molecules. Transferable Potentials for Phase Equilibria. 2. United-Atom Description of Branched Alkanes," The Journal of Physical Chemistry B **103**, 4508–4517 (1999).

[6]J. J. Potoff and D. A. Bernard-Brunel, "Mie Potentials for Phase Equilibria Calculations: Application to Alkanes and Perfluoroalkanes," The Journal of Physical Chemistry B **113**, 14725–14731 (2009).

[7]J. R. Mick, M. Soroush Barhaghi, B. Jackman, L. Schwiebert, and J. J. Potoff, "Optimized Mie Potentials for Phase Equilibria: Application to Branched Alkanes," Journal of Chemical & Engineering Data **62**, 1806–1818 (2017).

[8]A. Hemmen and J. Gross, "Transferable Anisotropic United-Atom Force Field Based on the Mie Potential for Phase Equilibrium Calculations: n-Alkanes and n-Olefins," The Journal of Physical Chemistry B **119**, 11695–11707 (2015).

[9]D. Weidler and J. Gross, "Individualized force fields for alkanes, olefins, ethers and ketones based on the transferable anisotropic Mie potential," Fluid Phase Equilibria **470**, 101–108 (2018).

[10]W. Damm, A. Frontera, J. Tirado–Rives, and W. L. Jorgensen, "OPLS all-atom force field for carbohydrates," Journal of Computational Chemistry **18**, 1955–1970 (1997).

[11]W. L. Jorgensen, D. S. Maxwell, and J. Tirado-Rives, "Development and Testing of the OPLS All-Atom Force Field on Conformational Energetics and Properties of Organic Liquids," Journal of the American Chemical Society **118**, 11225–11236 (1996).

[12]S. W. I. Siu, K. Pluhackova, and R. A. Böckmann, "Optimization of the OPLS-AA Force Field for Long Hydrocarbons," Journal of Chemical Theory and Computation **8**, 1459–1470 (2012).

[13]M. L. P. Price, D. Ostrovsky, and W. L. Jorgensen, "Gas-phase and liquid-state properties of esters, nitriles, and nitro compounds with the OPLS-AA force field," Journal of Computational Chemistry **22**, 1340–1352 (2001).

[14]H. Sun, "COMPASS: An ab Initio Force-Field Optimized for Condensed-Phase ApplicationssOverview with Details on Alkane and Benzene Compounds," The Journal of Physical Chemistry B **102**, 7338–7364 (1998).

[15]W. Zhang and A. C. T. van Duin, "Improvement of the ReaxFF Description for Functionalized Hydrocarbon/Water Weak Interactions in the Condensed Phase," The Journal of Physical Chemistry B **122**, 4083–4092 (2018).

[16]B. H. Morrow and J. A. Harrison, "Evaluating the Ability of Selected Force Fields to Simulate Hydrocarbons as a Function of Temperature and Pressure Using Molecular Dynamics," Energy & Fuels **35**, 3742 – 3752 (2021).

[17]R. A. Messerly, M. C. Anderson, S. M. Razavi, and J. R. Elliott, "Mie 16–6 force field predicts viscosity with faster-than-exponential pressure dependence for 2,2,4-trimethylhexane," Fluid Phase Equilibria **495**, 76–85 (2019).

[18]K. D. Papavasileiou, L. D. Peristeras, A. Bick, and I. G. Economou, "Molecular Dynamics Simulation of Pure n-Alkanes and Their Mixtures at Elevated Temperatures Using Atomistic and Coarse-Grained Force Fields," The Journal of Physical Chemistry B **123**, 6229–6243 (2019).

[19]I. J. Prentice, X. Liu, O. A. Nerushev, S. Balakrishnan, C. R. Pulham, and P. J. Camp, "Experimental and simulation study of the high-pressure behavior of squalane and poly-α-olefins," The Journal of Chemical Physics **152**, 074504 (2020).

[20]A. Einstein, "Über die von der molekularkinetischen Theorie der Wärme geforderte Bewegung von in ruhenden Flüssigkeiten suspendierten Teilchen," Annalen der Physik **322**, 549–560 (1905).

[21]S. J. Marrink, H. J. Risselada, S. Yefimov, D. P. Tieleman, and A. H. de Vries, "The MARTINI Force Field: Coarse Grained Model for Biomolecular Simulations," The Journal of Physical Chemistry B **111**, 7812–7824 (2007).